INTERNATIONAL JOURNAL OF INTEGRATED ENGINEERING
ISSN: 2229-838X e-ISSN: 2600-7916

IJIE

Vol. 16 No. 1 (2024) 135-142
https://publisher.uthm.edu.my/ojs/index.php/ijie

Nanostructuring of Additively Manufactured 316L Stainless Steel via High-Pressure Torsion for Enhanced Strength and Corrosion Performance

Shahir Mohd Yusuf[1]*, Nong Gao[2]

[1] *Engineering Materials and Structures (eMast) iKohza, Malaysia-Japan International Institute of Technology (MJIIT), UTM Kuala Lumpur, 54100 Kuala Lumpur, MALAYSIA*
[2] *Materials Research Group, Mechanical Engineering Department, Faculty of Engineering and Physical Sciences, University of Southampton, Southampton SO17 1BJ, UNITED KINGDOM*

*Corresponding Author: shahiryasin@utm.my
DOI: https://doi.org/10.30880/ijie.2024.16.01.011

Article Info

Received: 17 November 2023
Accepted: 13 January 2024
Available online: 28 April 2024

Keywords

Nanostructuring, additive manufacturing, high-pressure torsion, 316L stainless steel, strength, corrosion performance

Abstract

Bulk nanostructured materials (BNM) are defined as metallic materials with grain sizes <100 nm and are known to possess superior mechanical and functional properties compared to those with grain sizes in the micron and millimeter ranges. In this study, high-pressure torsion (HPT), a nanostructuring approach that imposes compressive stress and extreme torsional strain on bulk materials is applied to an additively manufactured (AM) 316L stainless steel (316L SS) for 10 revolutions. The grain sizes, hardness, and corrosion performance before and after HPT are evaluated by using extensive microscopy techniques, Vickers hardness (HV) measurements, and electrochemical tests conducted in 3.5 wt.% NaCl solution, respectively. The results show that after 10 HPT revolutions, nano-sized grains (average: ~42 nm) are obtained, whereas a three-fold increase in HV values from ~220 HV to ~600 HV are observed. Furthermore, the corrosion performance is also significantly enhanced as indicated by the reduction in corrosion rate from 2.53 μm/year initially, to 0.48 μm/year after HPT processing. These results highlight the benefits of HPT in producing bulk nanostructured materials with remarkably high hardness and excellent corrosion performance, potentially useful for a myriad of applications.

1. Introduction

Nanoengineering is an engineering discipline that involves the manipulation and interaction of nanostructures in the atomic and/or molecular scales (10^{-9} nm or less) to produce materials, devices, or systems possessing entirely new/programmable functionalities and capabilities [1]. Some examples of nanomaterials that result from nanoengineering are carbon nanotubes (CNT), semiconductors, and microelectromechanical systems (MEMS). CNTs have high strength-to-weight ratio and excellent thermal conductivity, which are incorporated in various sports equipment to improve performance and durability. In addition, semiconductor devices find their application in various electrical and electronics equipment, such that they are used as single discrete devices or as integrated circuit (IC) chips. Moreover, MEMS devices are also used for similar applications as semiconductor devices, but they are tiny integrated devices/systems in the sub-micron scale (<1 μm), that combine mechanical and electrical components within a single component. Precision engineering techniques including

photolithography (PL), electron beam lithography (EBL), nanoimprint technology (NIL), and micro-machining are commonly used to produce such nanomaterials and nanodevices [2]. These techniques fall under the subtractive manufacturing (SM) category, in which high-energy beams (PL, EBL, and NIL) and precision cutting tools (micromachining) are used to remove some parts/sections of a bulk material to achieve the desired shapes and structures.

On the other hand, bulk nanostructured materials (BNMs) are a class of metals and alloys having grain sizes ≤100 nm with superior mechanical (e.g. tensile strength and superplasticity) and functional (e.g. corrosion and wear) properties than their coarse-grained counterparts [3–5]. Such BNMs are typically produced via a nanostructuring approach termed severe plastic deformation (SPD), in which extremely high strains are imparted on bulk metallic materials to cause significant microstructural refinement that often results in improvement of the properties [6,7]. High-pressure torsion (HPT) is an SPD technique that involves the application of combined compressive force and torsional strain on thin disks (~1 mm thick) under high pressure (up to 6 GPa) via upward movement and rotation/revolution of the lower anvil of the HPT machine, respectively. It is one of the most effective SPD techniques in producing large volume fractions of high-angle grain boundaries (GBs), thereby enabling the grain refinement level and homogeneity of strain distribution to be controlled by varying the number of revolutions of the lower anvils [8,9]. Therefore, HPT can be regarded as a nanostructuring approach within the realm of nanoengineering to produce nanomaterials.

Therefore, in this study, HPT processing through 10 revolutions is applied to produce nanostructures in a 316L stainless steel (316L SS) alloy additively manufactured (AM) by laser powder bed fusion (L-PBF), followed by hardness and corrosion resistance tests to evaluate the mechanical and functional properties of the nanostructured material, respectively. L-PBF is an additive manufacturing process that uses laser beam to selectively melt and fuse successive powder layers to form a 3D object based on the initial computer aided design (CAD) data. L-PBF AM 316L SS is selected to be subjected to HPT in this study because L-PBF AM is known to produce novel microstructures comprising of melt pools, cellular structures, and fine grain sizes down to 10 µm, and due to its ability to tailor these microstructures to suit the required applications by varying the processing parameters [10–12]. Additionally, 316L SS is chosen as it is an engineering alloy widely used for various applications in the marine, biomedical, and nuclear industries. Thus, the combination of L-PBF AM and HPT in this study is expected to yield unique nanostructural features that result in superior strength and corrosion performance for the targeted alloy.

2. Materials and Experimental Procedures

Spherical gas-atomised 316L SS powder with particle sizes ranging from 5 – 55 µm supplied by Concept Laser GmbH were used in this study. Electron dispersive x-ray spectroscopy (EDX) analysis reveal the following chemical composition for the 316L SS powder (in wt.%): Cr: 18.43, Ni: 12.2, Mo: 2.46, Si: 0.75, P: 0.032, C: 0.02 S: 0.01, and Fe: *bal*. On the other hand, x-ray diffraction (XRD) measurements showed that the powder consists of a single γ-austenite phase.

L-PBF additive manufacturing of a 200 mm long cylindrical rod with a diameter of 10 mm was conducted using a Concept Laser M2 Selective Laser Melting (SLM) machine. The following processing parameters were used for this process as recommended by Concept Laser: laser power, P: 200 W fiber laser, scan speed, v: 1600 mm s^{-1}, layer thickness, h: 30 µm, hatch spacing, s: 150 µm, and 5 x 5 mm^2 'island' scan strategy. The build environment was purged with nitrogen to prevent contamination and oxidation, while the internal temperature was kept at 21°C throughout the SLM process. The rod was built vertically upright parallel to the z-direction.

The cylindrical rod was then machined to a diameter of 9.8 mm and then sliced into thin disks of thickness ~1 mm before being ground to thicknesses ranging from 0.81 – 0.86 mm. HPT processing was then conducted using a HPT facility at room temperature, such that the thin disks were placed inside a circular depression located in the middle of the upper and lower anvils of the HPT facility. The disks were deformed via the upward movement of the lower anvil that provided compressive force, subsequently followed by its rotation that imposed extreme torsional strains. The disk samples were subjected to a pressure of 6 GPa and constant rotational speed of 1 rpm for 10 revolutions. The equivalent von mises strain imposed by HPT, ε_{HPT} can be estimated by the following equation [13]:

$$\varepsilon_{HPT} = \frac{2\pi NR}{h\sqrt{3}} \quad (1)$$

where N is the number of HPT revolutions (N=10 in this study), R is the distance from the centre, and h is the initial disk thickness. Based on Eqn. 1, the HPT-imposed equivalent von mises strain were evaluated as 136.

The as-received and HPT-processed disks through 10 revolutions were then subjected to typical sample preparation procedures for scanning electron microscopy (SEM) and electron backscattered diffraction (EBSD) observations detailed in Ref. [14] and for transmission electron microscopy (TEM) described in Ref. [15]. The

Int. Journal of Integrated Engineering Vol. 16 No. 1 (2024) p. 135-142

microstructural features before and after HPT processing such as melt pools, cellular structures, grain sizes, and dislocations were characterised using these extensive microscopy techniques.

Vickers microhardness (HV) measurements were taken: (i) along the diameter of the disks with a distance of 0.6 mm between the main indents, with further 4 indents spaced at 0.3 mm around each main indent and (ii) throughout the surface of the thin disks in a rectilinear grid pattern to evaluate the hardness evolution along the diameter disk and hardness homogeneity throughout the disk, respectively. Both types of HV measurements were conducted using Future Tech FM-300 Vickers hardness testing machine under an applied load of 100 gf with a dwell time of 15 s.

For corrosion testing, a three-electrode electrochemical cell was immersed in a 3.5 wt.% NaCl solution with a Gamry Reference 600 potentiostat. The electrodes consist of the following: (i) Teflon sample holder that placed the thin disks as working electrode, (ii) Ag/AgCl electrode in 3.5 M KCl solution as reference electrode, and (iii) graphite rod as counter electrode. The corrosion tests were conducted in a Faraday Cage at room temperature to prevent vibrations and noises that can be induced from nearby movements, which may affect the test results. The thin disks were firstly held inside the 3.5 wt.% NaCl solution for 1 hour to achieve a quasi-steady open-circuit potential (OCP). Potentiodynamic polarisation (PP) behaviour was then assessed over a range of -0.2 V to 1.5 V against the OCP at a scan rate of 0.17 mV s^{-1}. Finally, the corroded as-received and HPT-processed disks were subjected to SEM observations to qualitatively evaluate and correlate with the quantitative results obtained from the OCP and PP tests to determine the influence of HPT processing on the corrosion performance of L-PBF AM 316L SS.

3. Materials and Experimental Procedures

3.1 Microstructural Evolution

Figs. 1(a) and (b) show representative images of the microstructures attained for 316L SS through L-PBF AM processing. A mix of coarse and fine grains averaging 40 ±30 μm can be observed in a square-like pattern, also termed melt pools that forms due to the 'island' or checkerboard sign strategy (Fig. 1(a)). The fine grains are particularly concentrated at the junctions of the melt pools, which result from the rapid change of laser scanning path direction that restrict grain growth and promotes multiple grain nucleation within a single melt pool [16,17]. SEM observations at higher magnification reveal equiaxed cellular structures in the sub-micron range, i.e. <1 μm growing through the melt pools and grain boundaries (Fig. 1(b)). These honeycomb-like cells resemble the microstructure of laser welded structure that typically form due to the rapid heating/cooling cycles during the process [18]. However, the cells formed in L-PBF AM structures are much smaller than their laser welded counterparts due to the higher solidification rate in L-PBF AM process (105 – 107 K s^{-1}) compared to that in laser welding (103 – 105 K s^{-1}) [19]. After 10 HPT revolutions, the cellular structures are completely annihilated due to the extreme torsional strain imposed during HPT processing as displayed in Fig. 1(c). Similarly, the grain boundaries could no longer be resolved through EBSD, which suggest that the grains may have been significantly refined into the sub-micron or even nano-scale region. Indeed, the bright field and dark field TEM images in Figs. 1(d) and (e), respectively exhibit equiaxed nano-sized grains with clear and distinct grain boundaries (average: 42 ± 10 nm). Dense dislocation networks can also be observed within some of the grain interior, while some of the grains are free from internal sub-structures (Fig. 1(d)). The formation of nano-scale grains and the presence of dense dislocation within the interior of some grains after 10 HPT revolutions can be attributed to the competing hardening and softening phenomenon, as well as the balance in dislocation nucleation and elimination as a result of plastic shearing due to the extreme HPT-imposed torsional strain [20–23].

3.2 Hardness

Fig. 2(a) shows the variation in HV values with respect to the indentation locations across the diameter of the disks, in which ~3-fold increase in microhardness is attained from ~220 HV before HPT processing to ~600 HV after 10 HPT revolutions. The remarkable increase in HV values can be ascribed to the nano-scale grain boundaries and dense dislocation networks that become effective sites to impede dislocation motions, generated as a result of extreme torsional strain imparted by HPT processing [24–26], and is typical of HPT-processed metals and alloys that exhibit strong strain hardening capabilities without recovery subjected to extremely high torsional strains [27–29]. On the other hand, the colour-coded contour maps in Figs. 2(b) reveal homogeneous hardness distribution throughout the disk surface after 10 HPT revolutions. This is interesting because Eqn. 1 estimates that there should be a radial dependency in terms of the HPT-imposed torsional strain levels, such that the central disk region (0 – 2.5 mm from the disk centre) should experience lower strains compared to the peripheral areas (>2.5 mm from the disk centre). Thus, the central area of the disk should exhibit lower hardness compared to that at the disk periphery, but the results of this study show relatively similar hardness values throughout the disk surface. Actually, this phenomenon is termed 'saturation' and has also been observed in other metals and alloys

processed by HPT, such that the work hardening rate decreases with increasing number of HPT revolution until it reaches a 'saturated' state upon a critical torsional strain value [27,30,31], ε_{HPT}= 136 (N=10) in this study.

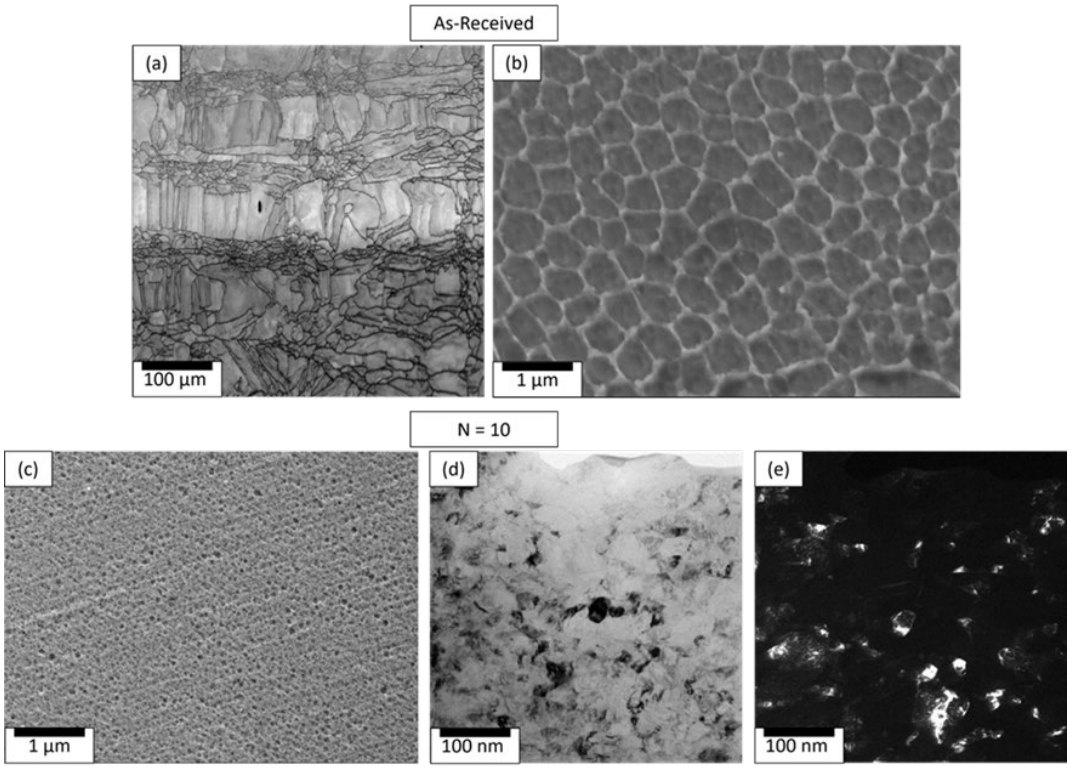

Fig. 1 *Microstructures of as-received samples (a) and (b); and microstructures after 10 HPT revolutions (c) – (e)*

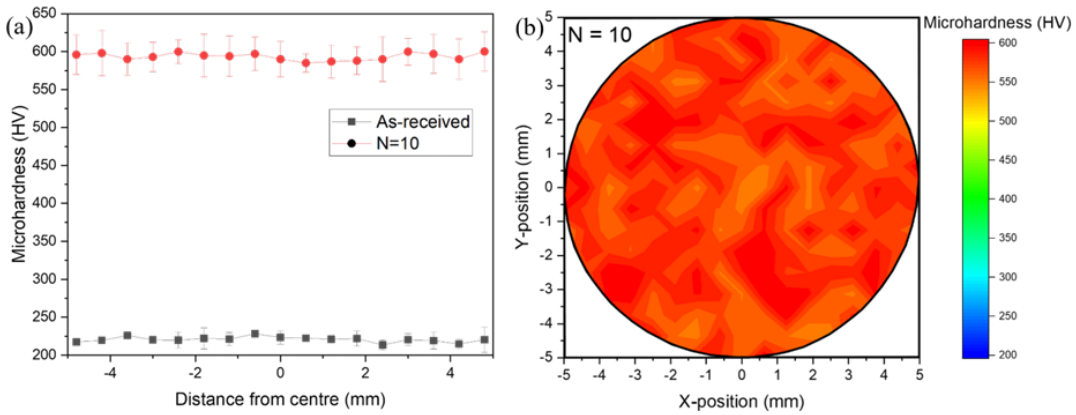

Fig. 2 *HV measurements (a) across the diameter; and (b) throughout the surface of the as-received and HPT-processed disks*

3.3 Corrosion Performance

Potentiodynamic polarisation (PP) test is a well-known approach that enables quantitative evaluation of the corrosion performance of a material in a certain environment. The resulting PP curves of the as-received and HPT-processed disks immersed in a 3.5 wt.% NaCl solution are shown in Fig. 3. Subsequently, Tafel fitting was conducted on the PP curves to extract various corrosion performance parameters such as corrosion current density, i_{corr}, that is used to calculate the corrosion rate, and pitting potential, E_{pit}, all of which are determined using the Gamry Echem software based on the ASTM G102-189 standard [32]. The results of Tafel fitting are displayed in Table 1.

Int. Journal of Integrated Engineering Vol. 16 No. 1 (2024) p. 135-142

Table 1 *Corrosion performance parameters from PP test*

Sample	i_{corr} (μA cm^{-2})	Corrosion rate (μm year^{-1})	E_{pit} (mV)
As-received	0.0616±0.0151	2.53±0.62	256±5
N=10	0.0117±0.0005	0.48±0.21	984±8

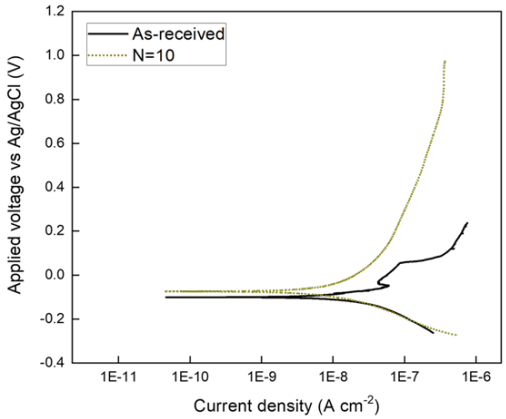

Fig. 3 *Representative SEM images of the worn samples (a) before HPT processing; and (b) after 10 HPT revolutions*

Based on Fig. 3 and Table 1, it is obvious that the i_{corr} value, and thus the corrosion rate after 10 HPT revolutions is lower than those of the as-received counterpart, thereby suggesting enhanced corrosion performance after HPT processing. On the other hand, the E_{pit} value of the disk subjected to 10 HPT revolutions is significantly higher than the as-received disk, implying reduced susceptibility to pitting corrosion [33]. In addition, SEM observations are also conducted on the surface of the corroded disks to gain further insight on the corrosion behaviour in the as-received and HPT-processed disks. Fig. 4(a) shows a large and deep crevice formed on the corroded as-received disk surface (solid circle), which could be due to the inability of the protective oxide layer on the surface of 316L SS to re-passivate as a result of lack of oxygen [34,35]. Corroded pits are also observed within the vicinity of the crevice, which suggests that the pits begin to grow from and scatter near the crevice area [36,37]. However, the surface of the disk subjected to 10 HPT revolution exhibit considerably smaller and shallower crevice with less pits, implying better corrosion resistance (Fig. 4(b)).

The observed improvements on the corroded disk surfaces in Fig. 4 correlate well with the quantitative results from PP tests (Fig. 3 and Table 1), confirming HPT processing yields better corrosion performance for L-PBF AM 316L SS when immersed in 3.5 wt.% NaCl solution. The improvement in corrosion performance after HPT processing through 10 revolutions can be attributed to the nano-scale grain refinement in such passivating environment as 3.5 wt.% NaCl solution that accelerates the formation and adhesion of passive oxide layers on the base metal due to increased amounts of grain boundaries [38]. Apart from that, the extreme HPT-imposed torsional strain also results in dense dislocation networks and higher residual stress that provide more nucleation sites that promote the stability and intactness of the thin passive oxide films [39]. Overall, it can be inferred that the enhanced corrosion performance can be ascribed to the rapid development of thick and dense passive oxide layer induced by the nano-scale grain refinement attained via HPT processing.

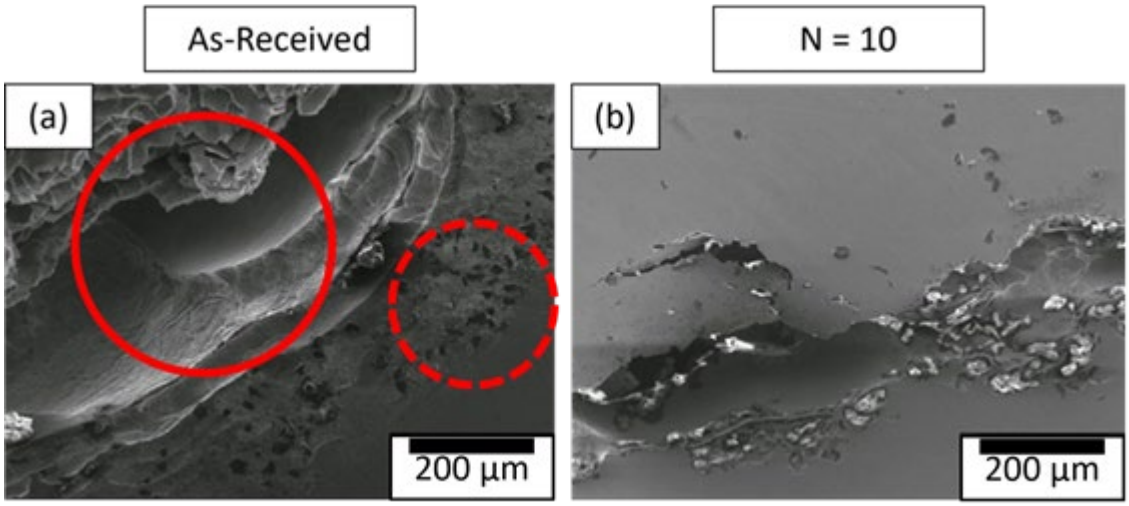

Fig. 4 *Representative SEM images of the worn samples (a) before HPT processing; and (b) after 10 HPT revolutions*

4. Conclusion

In this study, a nanostructured 316L SS fabricated by L-PBF AM was successfully attained by nanostructuring through HPT processing for 10 revolutions, followed by hardness and corrosion performance tests to evaluate the mechanical and functional properties. The following conclusions can be drawn based on the results of this study:

i. HPT processing yields exceptional grain refinement down to the nano-scale (average: ~42 nm) together with dense dislocation networks. Such microstructural refinement resulted in ~3-fold hardness increase as the immense grain boundaries and dislocations are effective sites to impede dislocation motions.
ii. 81% decrease of the corrosion rate and the observed much shallower crevice and less corroded pits after HPT processing provide evidence of enhanced corrosion performance in 3.5 wt.% NaCl solution. Such improvement in corrosion resistance is attributed to the accelerated production of thick and dense passive oxide layers due to the nano-scale grain refinement induced by HPT-imposed extreme torsional strain.
iii. Overall, the results of this study show the benefits of nanoengineering by nanostructuring through SPD to produce BNM with enhanced mechanical and functional properties that possess significant potential for various engineering and industrial applications.

5. Online License Transfer

By publishing in journals under Penerbit UTHM, the authors implicity transfers copyrights of their article to Penerbit UTHM. All authors are required to complete the Procedia exclusive license transfer agreement before the article can be published, which they can do online. This transfer agreement enables Penerbit UTHM to protect the copyrighted material for the authors, but does not relinquish the authors' proprietary rights. The copyright transfer covers the exclusive rights to reproduce and distribute the article, including reprints, photographic reproductions, microfilm or any other reproductions of similar nature and translations. Authors are responsible for obtaining from the copyright holder, the permission to reproduce any figures for which copyright exists.

Acknowledgement

This work was funded by the Ministry of Higher Education (MOHE) Malaysia under the Fundamental Research Grant Scheme (FRGS /1/2021/TK0/UTM/02/84).

Conflict of Interest

Authors declare that there is no conflict of interests regarding the publication of the paper.

Author Contribution

Study conception and design: *Shahir Mohd Yusuf and Nong Gao;* ***data collection:*** *Shahir Mohd Yusuf and Nong Gao;* ***analysis and interpretation of results:*** *Shahir Mohd Yusuf and Nong Gao;* ***draft manuscript preparation:*** *Shahir Mohd Yusuf, Nong Gao. All authors reviewed the results and approved the final version of the manuscript.*

References

[1] Jian, W., Hui, D., Lau, D. (2020). Nanoengineering in biomedicine: Current development and future perspectives. Nanotechnology Review, 9, 700–715. https://doi.org/10.1515/ntrev-2020-0053.

[2] Bayda, S., Adeel, M., Tuccinardi, T., Cordani, M., Rizzolio, F. (2020). The history of nanoscience and nanotechnology: From chemical-physical applications to nanomedicine. Molecules, 25(112), 1–15. https://doi.org/10.3390/molecules25010112.

[3] Valiev, R.Z., Zehetbauer, M.J., Hoppel, H.W., Ivanisenko, Y., Hahn, H., Wilde, G., Roven, H.J., Sauvage, X., Langdon, T.G. (2007). The innovation potential of bulk nanostructured materials. Advanced Engineering Materials, 9(7), 527–533. https://doi.org/10.1002/adem.200700078.

[4] Langdon, T.G. (2008). Processing of ultrafine-grained materials using severe plastic deformation: Potential for achieving exceptional properties. Revista de Metalurgia, 44(6), 556–564. https://doi.org/10.3989/revmetalm.0838.

[5] Valiev, R. (2004). Nanostructuring of metals by severe plastic deformation for advanced properties. Nature Materials, 3(8), 511–16. https://doi.org/10.1038/nmat1180.

[6] Edalati, K., Ashida, M., Horita, Z., Matsui, T., Kato, H. (2014). Wear resistance and tribological features of pure aluminum and Al-Al2O3 composites consolidated by high-pressure torsion. Wear, 3102014), 83–89. https://doi.org/10.1016/j.wear.2013.12.022.

[7] Estrin, Y., Vinogradov, A. (2013). Extreme grain refinement by severe plastic deformation: A wealth of challenging Science. Acta Materialia, 61(3), 782–817. https://doi.org/10.1016/j.actamat.2012.10.038.

[8] Edalati, K., Horita, Z. (2016). A review on high-pressure torsion (HPT) from 1935 to 1988. Materials Science and Engineering A, 652(2016), 325–352. https://doi.org/10.1016/j.msea.2015.11.074.

[9] Wongsa-Ngam, J., Kawasaki, M., Langdon, T.G. (2012). Achieving homogeneity in a Cu-Zr alloy processed by high-pressure torsion. Journal of Materials Science, 47(22), 7782–7788. https://doi.org/10.1007/s10853-012-6587-8.

[10] Sames, W.J., List, F.A., Pannala, S., Dehoff, R.R., Babu, S.S. (2016). The metallurgy and processing science of metal additive manufacturing. International Materials Reviews, 61(5), 1–46. https://doi.org/10.1080/09506608.2015.1116649.

[11] Attard, B., Cruchley, S., Beetz, C., Megahed, M., Chiu, Y.L., Attallah, M.M. (2020). Microstructural control during laser powder fusion to create graded microstructure Ni-superalloy components. Additive Manufacturing, 36(2020), 101432. https://doi.org/10.1016/j.addma.2020.101432.

[12] Olsen, J, Zhou, X, Zhong, Y., Liu, L., Wang, D., Yu, C., Wang, Y., Li, K., Xing, L., Ma, J., Cui, D., Liu, W., Shen, Z. (2017). Tailoring hierarchical structures in selective laser melted materials. IOP Conference Series: Materials Science and Engineering, 219(2017), 012036. https://doi.org/10.1088/1757-899X/219/1/012036.

[13] Jonas, J.J., Ghosh, C., Toth, L.S., (2014). The equivalent strain in high pressure torsion. Materials Science and Engineering A, 607(2014) 530–535. https://doi.org/10.1016/j.msea.2014.04.046.

[14] Mohd Yusuf, S., Zhao, X., Yang, S., Gao, N. (2020). Interfacial characterisation of multi-material 316L stainless steel/Inconel 718 fabricated by laser powder bed fusion. Materials Letters, 284(2021), 128928. https://doi.org/10.1016/j.msea.2014.04.046.

[15] Mohd Yusuf, S., Chen, Y., Yang, S., Gao, N. (2020) Microstructural evolution and strengthening of selective laser melted 316L stainless steel processed by high-pressure torsion. Materials Characterization, 159(2020), 110012. https://doi.org/10.1016/j.matchar.2019.110012.

[16] Pham, M.S., Dovgyy, B., Hooper, P.A. (2017). Twinning induced plasticity in austenitic stainless steel 316L made by additive manufacturing. Materials Science and Engineering A, 704(2017), 102–111. https://doi.org/10.1016/j.msea.2017.07.082.

[17] Tucho, W.M., Lysne, V.H., Austbø, H., Sjolyst-Kyerneland, Hansen. V. (2018). Investigation of effects of process parameters on microstructure and hardness of SLM manufactured SS316L. Journal of Alloys and Compounds, 740(2018), 910–925. https://doi.org/10.1016/j.jallcom.2018.01.098.

[18] Evin, E., Tomáš, M. (2017). The influence of laser welding on the mechanical properties of dual phase and trip Steels. Metals (Basel), 7(7), 1–16. https://doi.org/10.3390/met7070239.

[19] Gu, D.D., Meiners, W., Wissenbach, K., Poprawe, R. (2012). Laser additive manufacturing of metallic components: materials, processes and mechanisms. International Materials Reviews, 57(3), 133–164. https://doi.org/10.1179/1743280411Y.0000000014.

[20] Scheriau, S., Pippan, R. (2008). Influence of grain size on orientation changes during plastic deformation. Materials Science and Engineering A, 493(2008), 48–52. https://doi.org/10.1016/j.msea.2007.08.092.

[21] Scheriau, S., Zhang, Z., Kleber, S., Pippan, R. (2011). Deformation mechanisms of a modified 316L austenitic steel subjected to high pressure torsion. Materials Science and Engineering A, 528(2011), 2776–2786. https://doi.org/10.1016/j.msea.2010.12.023.

[22] Vorhauer, A., Pippan, R. (2004). On the homogeneity of deformation by high pressure torsion. Scripta Materialia, 51(9), 921–925. https://doi.org/10.1016/j.scriptamat.2004.04.025.
[23] Pippan, R., Wetscher, F. Hafok, M., Vorhauer, A. Sabirov, I. (2006). The limits of refinement by severe plastic Deformation. Advanced Engineering Materials, 8(11), 1046–1056. https://doi.org/10.1002/adem.200600133.
[24] Gubicza, J., El-Tahawy, M., Huang, Y., Choi, H., Choe, H., Lábár, J.L., Langdon, T.G. (2016). Microstructure, phase composition and hardness evolution in 316L stainless steel processed by high-pressure torsion. Materials Science and Engineering A. 657(2016), 215–23. https://doi.org/10.1016/j.msea.2016.01.057.
[25] Starink, M.J., Cheng, X., Yang, S. (2013). Hardening of pure metals by high-pressure torsion: A physically based model employing volume-averaged defect evolutions. Acta Materialia 61(2013) 183–192. https://doi.org/10.1016/j.actamat.2012.09.048.
[26] Enikeev, N.A., Sauvage, X., Abramova, M.M., Murashkin, M.Y., Valiev, R.Z. (2014). High strength state of UFG steel produced by severe plastic deformation. IOP Conference Series: Materials Science and Engineering. 63(2014), 012127. https://doi.org/10.1088/1757-899X/63/1/012127.
[27] Kawasaki,M., Lee, H.J., Ahn, B., Zhilyaev, A.P., Langdon, T.G. (2014), Evolution of hardness in ultrafine-grained metals processed by high-pressure torsion. Journal of Materials Research and Technology, 3(4), 311–318. https://doi.org/10.1088/1757-899X/63/1/012127.
[28] Tian, Y.Z., Wu, S.D., Zhang, Z.F., Figueiredo, R.B., Gao, N., Langdon, T.G. (2011). Strain hardening behavior of a two-phase Cu-Ag alloy processed by high-pressure torsion. Scripta Materialia, 65(6), 477–480. https://doi.org/10.1016/j.scriptamat.2011.06.004.
[29] Edalati, K., Fujioka, T., Horita, Z. (2009). Evolution of Mechanical Properties and Microstructures with Equivalent Strain in Pure Fe Processed by High Pressure Torsion. Materials Transactions, 50(2009), 44–50. https://doi.org/10.2320/matertrans.MD200812.
[30] Kawasaki, M., Figueiredo, R.B., Langdon, T.G. (2011). An investigation of hardness homogeneity throughout disks processed by high-pressure torsion. Acta Materialia, 59(1), 308–316. https://doi.org/10.1016/j.actamat.2010.09.034.
[31] Kawasaki, M. (2014) Different models of hardness evolution in ultrafine-grained materials processed by high-pressure torsion. Journal of Materials Science, 49(1), 18–34. https://doi.org/10.1007/s10853-013-7687-9.
[32] ASTM, ASTM G 102-89: Standard Practice for Calculation of Corrosion Rates and Related Information https://doi.org/10.1520/G0102-89R10.
[33] Mohd Yusuf, S., Nie, M., Chen, Y., Yang, S., Gao, N. (2018). Microstructure and corrosion performance of 316L stainless steel fabricated by Selective Laser Melting and processed through high-pressure torsion. Journal of Alloys and Compounds, 763(2018), 360–375. https://doi.org/10.1016/j.jallcom.2018.05.284.
[34] Zou J.X., Zhang, K.M., Hao, S.Z., Dong, C., Grosdidier, T. (2010). Mechanisms of hardening, wear and corrosion improvement of 316 L stainless steel by low energy high current pulsed electron beam surface treatment. Thin Solid Films, 519(4), 1404–1415. https://doi.org/10.1016/j.tsf.2010.09.022.
[35] Geenen, K., Röttger, A., Theisen, W. (2017). Corrosion behavior of 316L austenitic steel processed by selective
laser melting, hot-isostatic pressing, and casting. Materials and Corrosion, 9999, 1–12. https://doi.org/10.1002/maco.201609210.
[36] Sander, G., Thomas, S., Cruz, V., Jurg, M., Birbilis, N., Gao, X., Brameld, M., Hutchinson, C.R. (2017). On The Corrosion and Metastable Pitting Characteristics of 316L Stainless Steel Produced by Selective Laser Melting. Journal of The Electrochemical Society, 164(6) C250–C257. https://doi.org/10.1149/2.0551706jes.
[37] Lodhi, M.J.K., Deen, K.M., Greenlee-Wacker, M.C., Haider, W. (2019). Additively manufactured 316L stainless steel with improved corrosion resistance and biological response for biomedical applications. Additive Manufacturing, 27(2019), 8-19. https://doi.org/10.1016/j.addma.2019.02.005.
[38] Ralston, K.D., Birbilis, N. (2010). Effect of grain size on corrosion. Corrosion, 66(7), 075005-1–075005-13. https://doi.org/10.5006/1.3462912.
[39] Wang, X., Nie, M., Wang, C.T., Wang, S.C., Gao, N. (2015). Microhardness and corrosion properties of hypoeutectic Al-7Si alloy processed by high-pressure torsion. Materials and Design, 83(2015), 193–202. https://doi.org/10.1016/j.matdes.2015.06.018.